RESEARCH ARTICLE

Active Magnetic Bearing System Using I-Type and U-Type Actuator

UPAMA DAS[1], SUKANTA DEBNATH[1], SURAJ GUPTA[1], (Graduate Student Member, IEEE), PABITRA KUMAR BISWAS[1], (Member, IEEE), THANIKANTI SUDHAKAR BABU[2,3], (Senior Member, IEEE), AND NNAMDI I. NWULU[3], (Senior Member, IEEE)

[1]Department of Electrical and Electronics Engineering, National Institute of Technology Mizoram, Aizawl 796012, India
[2]Department of Electrical and Electronics Engineering, Chaitanya Bharathi Institute of Technology, Hyderabad 500075, India
[3]Centre for Cyber-Physical Food, Energy and Water Systems, University of Johannesburg, Johannesburg 2006, South Africa

Corresponding author: Thanikanti Sudhakar Babu (sudhakarbabu66@gmail.com)

ABSTRACT An active magnetic bearing (AMB) is an evolving research topic in the bearing industry. Compared to the conventional approach, AMB is more advantageous and has different industrial applications. The design of this bearing needs to be improvised to get more optimized performance. This leads us to focus on the better-designed structure of the actuator, which plays an essential role in AMB performance. Thus in this manuscript, we have designed and compared the I-type and U-type actuators' performances in terms of their resistance, inductance profile, and force profile to show the characteristics of these actuators. These designed actuators are simulated in Ansys Maxwell software, and compared with the simulation results. Further, these results are verified using hardware results, and the tested actuators are used to design two different AMB systems. One current controller is designed and simulated to achieve the stable levitated position of the rotor. This rotor is rotated by inserting an AC magnet in the system and finally, a rotational system is attained, and its speed is observed by the tachometer for both AMB systems. Both the proposed AMB systems are simple and compact in structure as these are having single coil and single power amplifier. These axial AMB systems are used in many high-speed applications as they are having features like less installation space, less cost and more room for heat dissipation.

INDEX TERMS Active magnetic bearing, controllers, hardware implementation, I-type and U-type actuator, magnetic analysis, load cell.

I. INTRODUCTION

Active Magnetic Bearing is an emerging bearing technology used in various industrial applications. Many AMB designs may be implemented and compared to obtain the best system. The actuator is the most significant component in designing an AMB system. Various types of actuators are available in the market, and an appropriate actuator selection is necessary to achieve better performance of the AMB system.

AMB systems transmit loads without lubrication utilizing electromagnetic forces. Avoiding the bearing lubrication system decreases the equipment footprint and removes expensive auxiliary equipment. AMBs require very little maintenance.

The associate editor coordinating the review of this manuscript and approving it for publication was Yingxiang Liu.

AMBs do not experience wear, but traditional bearings can have limited bearing life in running hours or start/stop cycles. Additionally, lubrication systems' high maintenance costs and ensuing downtime are eliminated with AMBs. AMB system intelligence also offers a variety of data on system stability and rotor forces. With the use of cutting-edge control algorithms, remote connectivity, and this data, it is possible to monitor, diagnose, and tune equipment without needing an expert.

The basic I and U topologies are popular choices for Active Magnetic Bearing (AMB) systems due to their simplicity, reliability, and effectiveness in controlling the position of a rotating mass.

The I topology consists of two sets of magnetic coils arranged parallel to the axis of rotation. The rotor is levitated

in the air gap between the two sets of coils, and the magnetic field is controlled to maintain the rotor's position.

The U topology is a modification of the I topology, where the two sets of coils are arranged in a U shape. This allows for a larger air gap between the rotor and the magnetic coils, resulting in increased stability.

When designing an AMB system for rotating masses, it is important to consider the perturbations caused by electric actuators and the radial forces they generate. The multidimensional nature of the system makes it more complex to control, but the I and U topologies are well-suited to handle these challenges.

The I and U topologies offer several advantages in this scenario. Firstly, they provide a non-contact method of support for the rotating mass, which eliminates the need for physical bearings that can wear out and generate heat. Secondly, they allow for very precise control of the position of the rotor, which is essential in applications where even slight deviations from the desired position can cause problems. Finally, the simple and robust design of these topologies makes them easy to maintain and repair, which is important for applications where downtime must be minimized.

In summary, the I and U topologies are excellent choices for AMB systems in rotating mass applications due to their simplicity, reliability, and effectiveness in controlling position, even in the presence of perturbations caused by electric actuators and radial forces [1], [2], [3], [4].

In this research area, various AMB structures are proposed, designed, and implemented. Like Du et al. presented an exact analytical method for active magnetic bearings to obtain the magnetic field distribution with rotor eccentricity. To obtain the displacement stiffness and current stiffness by calculating unbalanced magnetic force using Maxwell stress tensor theory [5]. Xu et al. proposed and developed a dynamic modelling method for the AMB system, considering both translational and rotational base motions based on a double-gimbal system model [6]. Further, Jiang et al. used distributed magnetic circuit method (DMCM) to calculate the initial flux density and magneto motive force (MMF) of each section by magnetic circuit calculation [7]. Heya et al. proposed a triaxial active control magnetic bearing (AMB) with an asymmetric structure. With a sensitivity function, stability against disturbances is evaluated [8]. Sun et al. suggested a vibration-suppression technique based on a generalised integrator and frequency locked loop (GI-FLL) and phase shift generalised integrator without an angular speed sensor (PSGI) [9]. In this study, Xu and Fang suggested a unique claw, a more compact radial construction active magnetic bearing (CAMB). This magnetic bearing has a claw-like shape because the stator core and coils are arranged along the axial direction of the bearing. This causes it to have a tiny radial extension that is approximately the same diameter as the rotor. The suggested magnetic bearing can be used when there is a lack of radial space [10]. Shyh-Leh Chen and Chan-Tang Hsu proposed a three-pole AMB.

It features fewer power amplifiers, less iron loss, and more room for heat dissipation, coil winding, and sensor installation than the eight-pole arrangement. The overall cost of the AMB might be decreased as a result. This research examines the robust stability of a voltage-controlled three-pole active magnetic bearing (AMB) system [11]. Chen and Weng explain that the system may experience both matched and mismatched uncertainty from several sources, including parametric delays caused by manufacturing and assembly defects and unmodeled magnetic forces generated by flux leakage. The method is an intriguing illustration supporting the back-stepping design [12]. Chen et al. proposed the imbalance adjustment for an AMB system with three poles. Based on immersion and invariance control (I&I) theory, a potential adaptive compensating technique is offered [13]. This study examines the robust control and system identification of a multi-input multi-output (MIMO) active magnetic bearing (AMB) system. The AMB system under investigation is open-loop unstable, and the existence of right-half plane zeros and the rotor flexible modes adds to the complexity of the control scheme for such a system [14]. This research examines the robust stability of a voltage-controlled three-pole active magnetic bearing (AMB) system. The system may experience both matched and mismatched uncertainty from a number of sources, including parametric uncertainties caused by manufacturing and assembly defects and unmodeled magnetic forces caused by flux leakage. The method serves as an intriguing illustration that supports the backstepping design but is not in the traditional rigorous feedback form [12]. A class of smooth feedback controllers for the stabilization of a three-pole active magnetic bearing (AMB) system is proposed in this study. The three-pole AMB system is substantially nonlinear and nonaffine. Traditional controllers are difficult to install and further research since they are complex and nonsmooth. A linear transformation of the system inputs is used to develop the suggested smooth controllers (coil currents) [15]. Here, present the results of an experimental investigation into a three-pole active magnetic bearing (AMB) system. Two cases—one including a motor and the other not—are looked at. A linear state feedback controller (LC), feedback linearization with a linear state feedback controller (FLLC), and feedback linearization with an integrated sliding mode controller were created and developed for the system without a motor (ISMC). We discovered that ISMC produces the greatest transient and steady-state performance, but both LC and FLLC would cause a limit cycle in the steady state [16].

This study shows that the variation in AMB system performance for different actuator shapes is still in its very first stage. This variation depends on many factors, like the shape of an actuator, the type of material, etc. Among the various available actuators, i.e., U, E, and I. Comparatively, I-type and U-type actuators are preferable over E-type. This E-type actuator has three lines of force; if the correct design is not implemented, these different lines of force will result in
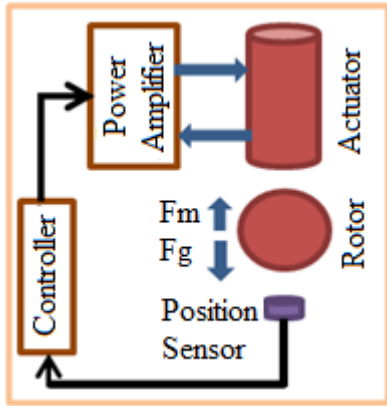
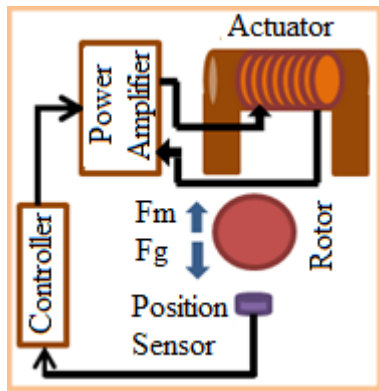**FIGURE 1.** Schematic diagram of I-type Active Magnetic Bearing.

FIGURE 2. Schematic diagram of U-type Active Magnetic Bearing.

TABLE 1. Specification of actuators and the rotors.

Actuator	I-type	U-type
Material used	CRGOS	CRGOS
Number of turns	700T	700T
Coil resistance	2.1 Ω	1.94 Ω
Coil Inductance	36 mH	30mH
Stack size	0.788 Inches	0.788 Inches
The gauge of insulated copper wire winding	19 SWG	20 SWG
Rotor:		
Rotor diameter	2cm	4cm
Rotor mass	50gm	65gm

to the power amplifier, and the power amplifier controls the actuator coil excitation current to sustain the rotor position [11], [12], [13], [17]. This paper represents a comparison to determine the performance of actuators as an AMB system. The attractive force and the Inductance profiles were compared between I-type and U-type actuators [18], [19], [20]. Based on the force and inductance data controller has been designed for both the AMB system [21], [22].

This manuscript presents two simple and compact structures for the AMB system. The proposed systems use only one coil for the design, which needs less power amplifier, less loss and even less space required. The overall cost of the AMB system can be decrease. Finally, a rotational system is designed to measure both the system and the bearing speed. This type of system can be used for high-speed applications.

II. ACTUATOR AND ROTOR DESIGN, ANALYSIS, AND TESTING

For designing a sound AMB system, actuator and rotor specifications are essential. The core loss depends on the actuator. For both I-type and U-type actuators, we choose Cold Rolled Grain Oriented Silicon Steel (CRGOS), in which core loss is less and the magnetic properties and magnetic properties also good, like high permeability, which allows more magnetic flux to flow. Specifications of I-type and U-type actuators and the rotating objects are given in table 1 [3].
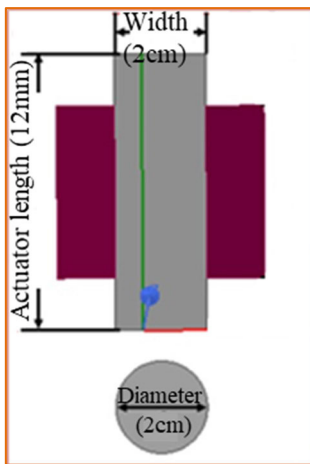
A. MAGNETIC ANALYSIS

A magnetic analysis has been done to determine the magnetic properties of both actuators. The ANSYS Maxwell FEM (Finite Element Method) platform determines the parameters. Figure 3 and figure 4 show the structure of the I-type and U-type actuators. Before analysis, we have to define the actuators and rotors' material properties, shown in table 2.

After selecting the material properties magnetic analysis has been done for ten different air gaps to check the different magnetic parameters for both the actuators. Vector plot of flux lines at 10mm air gap for I-type and U-type actuators are presented in figure 5 and figure 9. Figure 6 and figure 10 shows the vector plot of magnetic field intensity for both the actuators. Figure 7 and figure 11 shows the vector plot of magnetic flux density and figure 8 and figure 12 represents

non-uniform magnetic force. Since the leakage flux in I-type and U-type actuators is lower than in E-type actuators, the attractive force is higher. In this manuscript, analysis and testing have been done for both I-type and U-type actuators. It is observed that the I-type actuator has a more attractive force than the U-type actuator as the single line of force and leakage flux is less.

In this manuscript, we have discussed I-type and U-type actuators. Performance of the actuators' examined by determining the inductance and force profile. An actuator and the rotor are considered for determining these characteristics for a particular air gap. The air gap is crucial because as the air gap increases, the force and other values will decrease. For this experiment, ten different air gaps ranging from 1mm to 10mm is considered with a step of 1mm. Magnetic analysis and hardware tests have been done for both actuators' air gaps, and the results are compared [1], [2]. Based on the results, these actuators are used to design the proposed AMB system [3], [4].

Figure 1 and figure 2 represent the schematic diagram of the I-type and U-type AMB systems. Here rotor or object is suspended under the actuator, the position sensor senses the rotor position, and the position signal is sent to the controller [3], [10]. The controller directs a control signal

TABLE 2. Material properties for the actuators and rotors.

Name	Rotor (Iron)	Actuator (iron)	Coil (copper)	Units
Thermal conductivity	69	69	450	W/mK
Poisson's ratio	0.48	0.48	0.58	
Bulk conductivity	10300000	10300000	5800000	S/m
Relative Permeability	4000	10000	0.99	
Mass Density	7970	7970	8733	Kg/m3

FIGURE 3. Structural representation of I-type system (ANSYS).
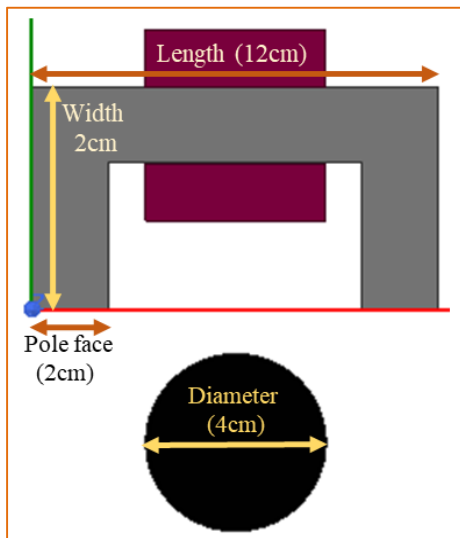
FIGURE 4. ANSYS structure of U-type actuator.

the vector plot of attractive force for I-type and U-type actuator.

The magnetic analysis data for ten different air gaps for both the actuators are observed and tabulated in the table 3 (for I-type) and table 4 (for U-type).
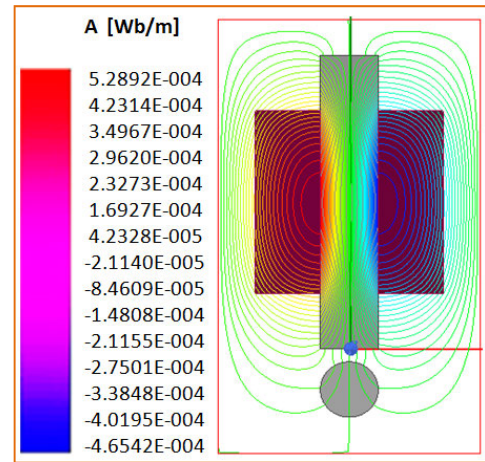
FIGURE 5. Vector plot of the I-type actuator's magnetic flux line for a 10 mm air gap.
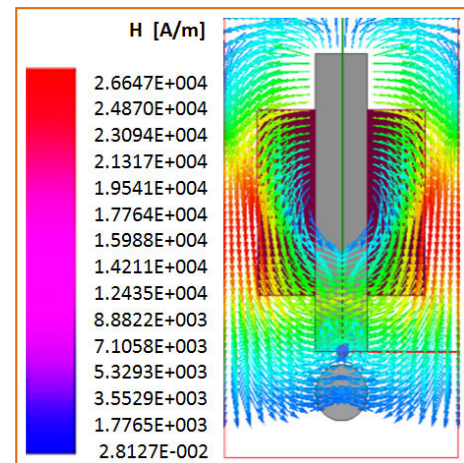
FIGURE 6. Vector plot result of the I-type actuator's Magnetic field intensity for 10mm air gap.
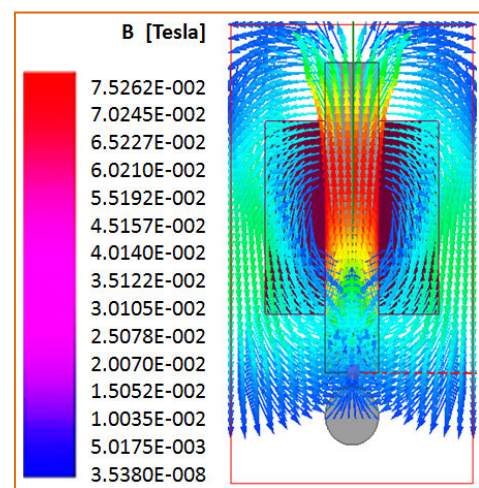
FIGURE 7. Vector plot of the I-type actuator's magnetic flux density for a 10 mm air gap.

A comparison of magnetic analysis results between I-type and U-type actuators has been made to differentiate the performance between them. The following figure shows the

TABLE 3. Magnetic analysis data of the ten different air gaps for I-type actuator.

Air gap (mm)	Flux line (Wb/m)	Magnetic flux density(B)T	Magnetic field(H)A/m	Inductance (mH)	Force (N)
1	5.2962E-4	8.9863E-2	3.00E+04	37.78	335.654
2	5.2926E-4	8.5483E-2	2.97E+04	37.45	286.766
3	5.2904E-4	8.0252E-2	2.85E+04	37.12	256.876
4	5.2899E-4	7.8536E-2	2.73E+04	36.75	241.235
5	5.2892E-4	7.5262E-2	2.66E+04	36.47	227.757
6	5.2877E-4	7.8550E-2	2.59E+04	36.11	209.644
7	5.1875E-4	6.9348E-2	2.48E+04	35.76	187.644
8	4.9868E-4	6.7359E-2	2.33E+04	35.54	153.986
9	4.8855E-4	6.1531E-2	2.20E+04	35.27	127.677
10	4.2842E-4	5.4362E-2	2.05E+04	35.03	105.648

TABLE 4. Magnetic analysis data for the ten different air gaps for U-type actuator.

Air gap in mm	Flux line (Wb/m)	Magnetic flux density(B)T	Magnetic field (H)A/m	Inductance (mH)	Force (N)
1	4.4717E-004	5.6238E-002	2.90E+04	36.54	221.343
2	4.3673E-004	5.3286E-002	2.75E+04	36.12	203.341
3	4.2832E-004	5.0876E-002	2.52E+04	35.71	187.434
4	3.7136E-004	4.8468E-002	2.39E+04	35.43	172.342
5	3.1193E-004	4.4236E-002	2.24E+04	35.03	150.564
6	3.0635E-004	4.1356E-002	2.02E+04	34.87	127.432
7	2.9986E-004	3.8659E-002	1.83E+04	34.12	114.242
8	2.8462E-004	3.2829E-002	1.61E+04	33.78	097.311
9	2.7295E-004	2.7531E-002	1.38E+04	33.11	081.231
10	2.5695E-004	2.3654E-002	1.18E+04	32.56	064.131
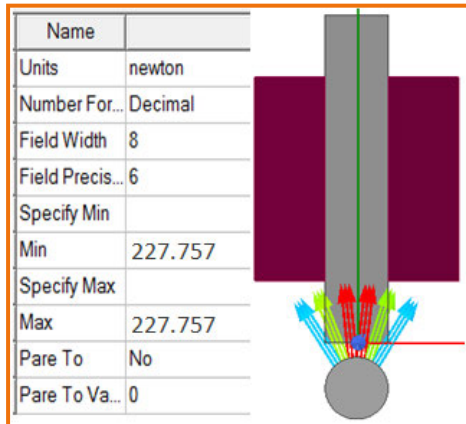
FIGURE 8. Vector plot result of the I-type actuator's attractive force.

FIGURE 9. Vector plot result of the U-type actuator's flux line for 10mm air gap.

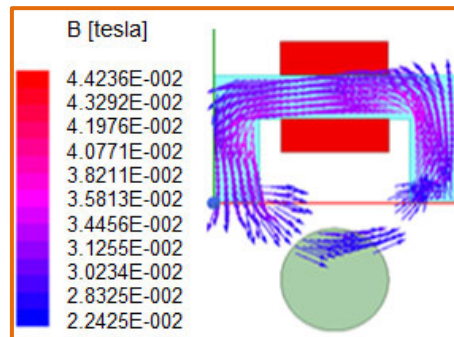**FIGURE 10.** Vector plot result of the U-type actuator's Magnetic field intensity for 10mm air gap.

behaviour of all the parameters and how these vary with the increase in the air gap.

Figure 13 shows the flux pattern comparison of I-type and U-type actuators and flux is decreasing as the air gap is increasing. Magnetic field strength is less for the U-type of actuator and decreasing with the increasing in air gap as presented in figure 14.

A comparison graph of magnetic flux density, inductance profile and attractive force profile for both the actuators are presented in figure 15, figure 16 and figure 17 respectively. From these three graphs it is observed that magnetic property of the I-type is better than U-type and the values are decreasing with the increasing in air gap.

B. ACTUATOR AND ROTOR DESIGN AND TESTING

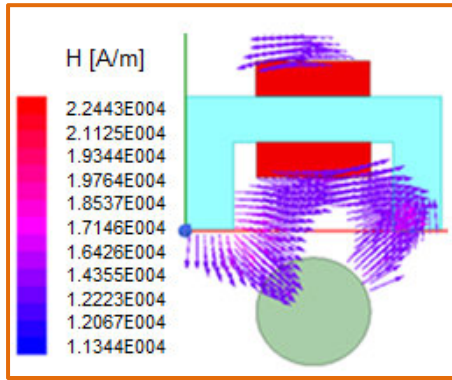I-type and U-type actuator structure is shown in figure 18 and Figure 19, and the design parameters according to this

FIGURE 11. Vector plot result of the U-type actuator's flux density for the 10 mm air gap.
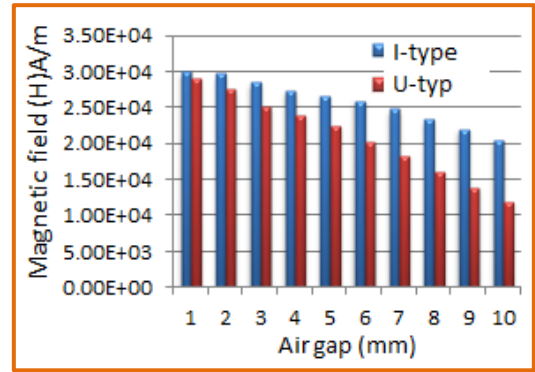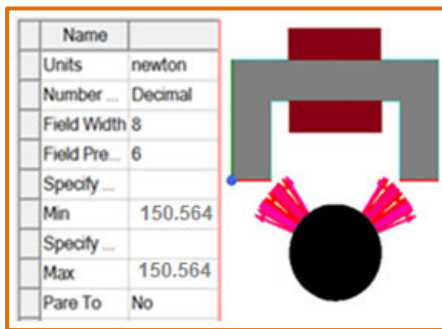

FIGURE 12. Vector plot result of the U-type actuator's Magnetic force.

FIGURE 13. Flux pattern comparison between I-type and U-type actuator.
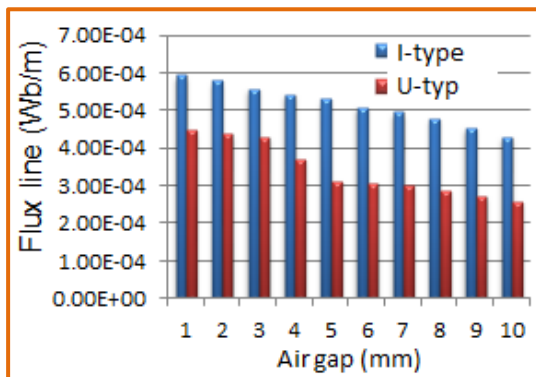

FIGURE 14. Magnetic field strength comparison between I-type and U-type actuators.

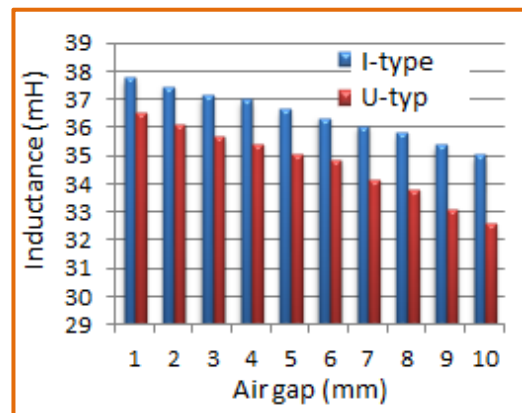**FIGURE 15.** Magnetic flux density comparison between I-type and U-type actuator.

FIGURE 16. Inductance profile comparison between I-type and U-type actuator.

structure are given in table 5. The fabricated actuators and rotors are shown in figure 20 and figure 21, respectively. The air gap between the actuator and rotor varies from 1mm to 10mm to check the actuator's performance [3].

1) DC TEST FOR RESISTANCE MEASUREMENT

These tests are performed to obtain the experimental resistances of both actuators. For these tests, supply is given to the actuator from a DC source through rheostat to control the voltage, as shown in figure 22 and figure 23. An ammeter and voltmeter are used to measure current and voltage for calculating resistance.

2) AC TEST FOR INDUCTANCE MEASUREMENT

These tests are performed to obtain the experimental inductance of both actuators. For these tests, supply is given to the actuator from an AC source through a rheostat to control the voltage, as shown in figure 24 and figure 25. Ammeter and voltmeter are used to measure current and voltage for calculating inductance.

3) ATTRACTIVE FORCE MEASUREMENT USING LOAD CELL TEST

This test determines the attractive force between the actuator and the rotor as shown in figure 26 and figure 27. The rotor
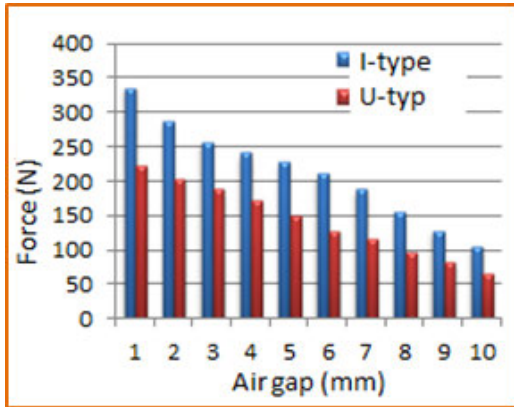
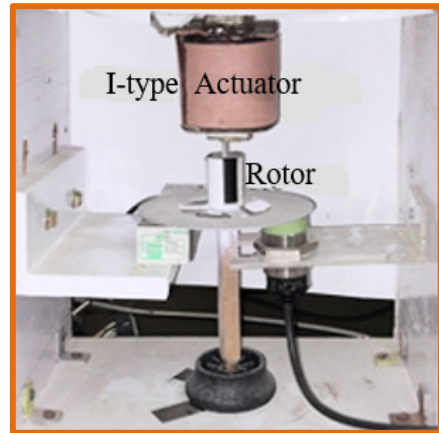**FIGURE 17.** Attractive force comparison between I-type and U-type actuators.

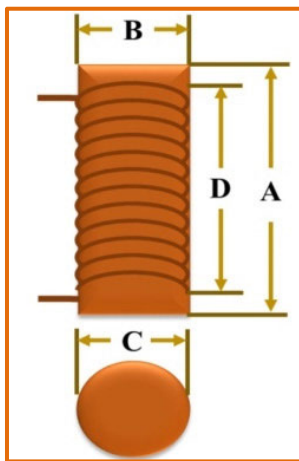**FIGURE 20.** Fabricated I-type AMB setup for experimental investigation.

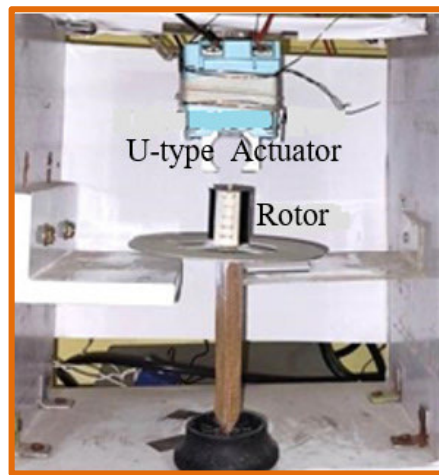**FIGURE 18.** Dimensional view of I-type actuator and rotor.

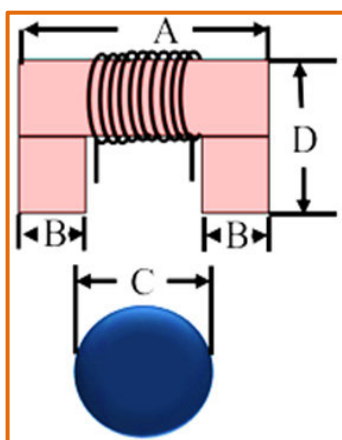**FIGURE 21.** Fabricated U-type AMB setup for experimental investigation.

TABLE 5. Measurement of actuators and rotors.

I-type actuator		U-type actuator	
Parameter	Dimension	Parameter	Dimension
A	12cm	A	12cm
B	2cm	B	2cm
C	2cm	C	4cm
Core thickness	2cm	D	10cm
Rotor Weight	50gm	U-type core thickness	2cm
		Weight of the rotor	65gm

FIGURE 19. Dimensional view of U-type actuator and rotor.

which converts the attractive force into grams and displays it in the LCD's output.

III. EXPERIMENTAL COMPARISON OF ACTUATORS
Experimental determination is vital for any analysis, and we can get accurate results. In this paper, an experimental comparison has been made between I-type and U-type actuators to analyse actuators.
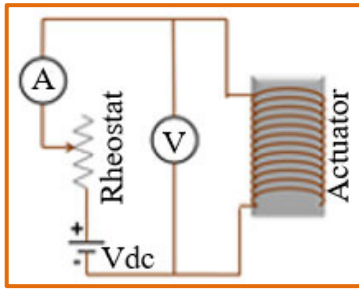
is fixed with the load cell to do the force measurement. When the supply is fed to the actuator, it produces the attractive force, and that force is observed by the load cell. The force sensed by the load cell is provided to the microcontroller,

FIGURE 22. DC test without an object for I-type actuator.

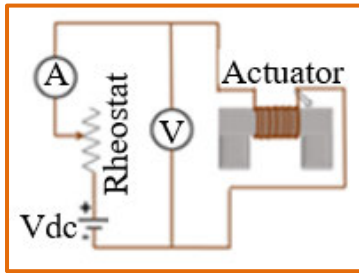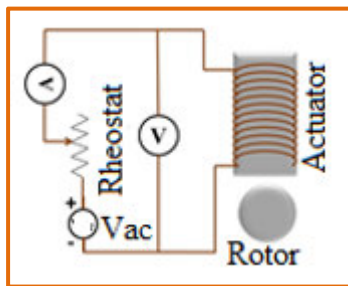**FIGURE 23.** DC test without an object for U-type actuator.

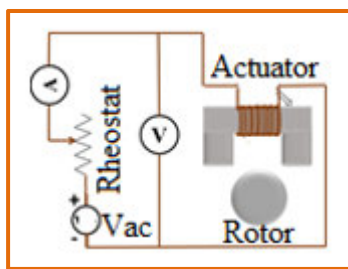**FIGURE 24.** AC test with the object for I-type actuator.

FIGURE 25. AC test with the rotor for U-type actuator.

For the comparison, three hardware setup is prepared, one for resistance measurement, one for inductance measurement, and one more set up for attractive force measurement.

The hardware setup for resistance measurement for both actuators is shown in figure 28 and figure 29. Two multimeters are used for voltage and current measurement; then, resistance is calculated and tabulated in table 6 for both actuators. For 11 different voltages, resistance is measured, and the mean value of resistance is given below.
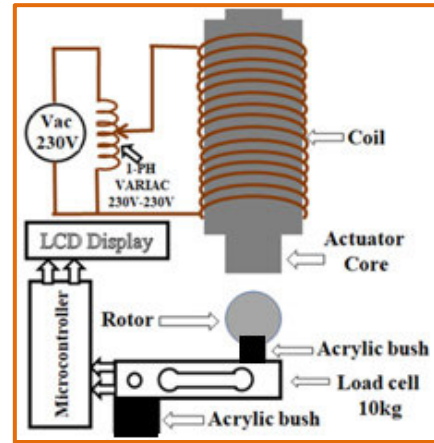

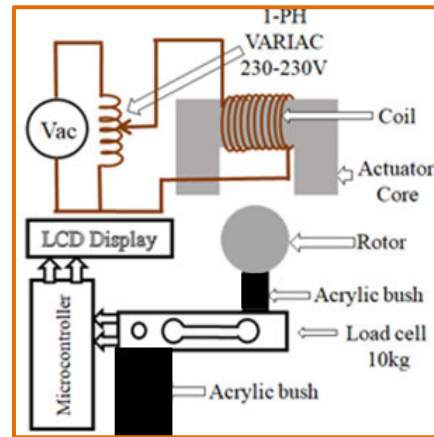**FIGURE 26.** Attractive force measurement for I-type actuator using Load cell test.

FIGURE 27. Attractive force measurement for U-type actuator using Load cell test.

TABLE 6. I-type and U-type actuator experimental data of DC Test for Resistance measurement.

Sl. No.	Voltage (V)		Current (A)		Resistance (Ω)	
	I-type	U-type	I-type	U-type	I-type	U-type
1	1.0	1.0	0.516	0.676	1.930	1.479
2	1.5	1.5	0.769	0.925	1.950	1.622
3	2.0	2.0	1.040	1.578	1.920	1.267
4	2.5	2.5	1.290	1.986	1.930	1.259
5	3.0	3.0	1.550	2.142	1.935	1.401
6	3.5	3.5	1.800	2.453	1.944	1.426
7	4.0	4.0	2.050	2.802	1.951	1.427
8	4.5	4.5	2.300	3.125	1.956	1.440
9	5.0	5.0	2.550	3.414	1.960	1.465
10	5.5	1.0	2.800	3.705	1.964	1.484
11	6.0	1.5	3.040	3.953	1.973	1.517

The mean value of resistance are Resistance for I-type actuator

$$R_{I-type} = \frac{R_n}{n} = \frac{21.413}{11} = 1.946\Omega$$

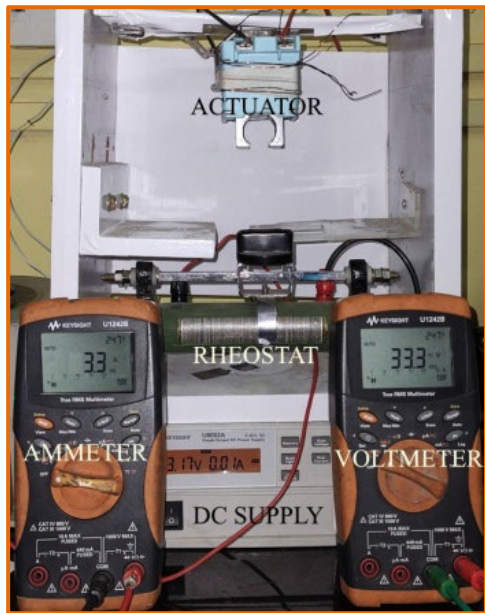**FIGURE 28.** Hardware setup for resistance measurement for I-type actuator.

FIGURE 29. Hardware setup for resistance measurement for U-type actuator.

Resistance for U-type actuator

$$R_{U-type} = \frac{R_n}{n} = \frac{15.787}{11} = 1.435\,\Omega$$

Figure 30 and figure 31 present the experimental setup for inductance measurement. In this setup, two multimeters are used as voltmeters and ammeters, and one variac is used for varying the supply voltage. These tests have been done for ten different air gaps. For a particular air gap, three different

FIGURE 30. Experimental setup for inductance measurement for I-type actuator.
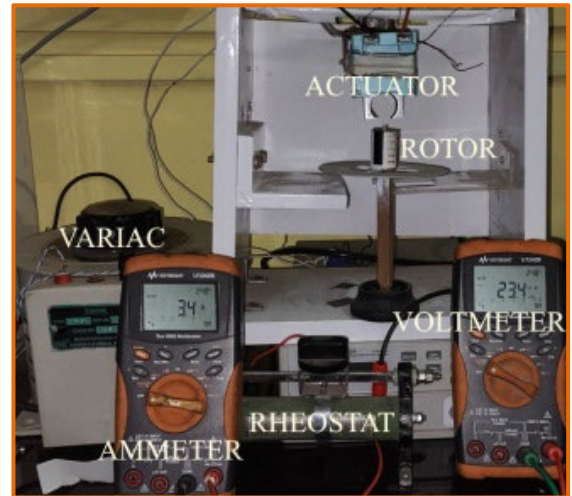

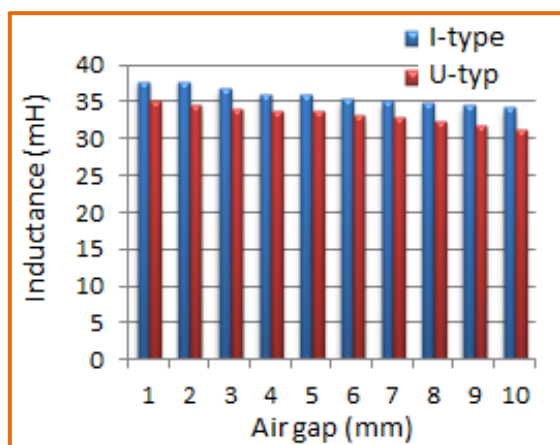**FIGURE 31.** Experimental setup for inductance measurement for U-type actuator.

voltages and currents are taken. Three inductance values are calculated using these values, and the average value is tabulated in Table 7 for both actuators.

From the data shown in table 7, the characteristics graph has been drawn and shown in figure 32. These inductance profiles show that the I-type actuator has a higher value for all the air gaps.

For the attractive force measurement, the object or rotor is fixed with the 10kg load cell as shown in figure 33 and figure 34; when the variac actuator increases, the supply voltage generates the attractive force and attracts the rotor, and that force is experienced by the load cell. The LCD is connected to the load cell through a microcontroller and displays the gram's attractive force. The experimental results are given in Table 8, and the performance graph for ten air gaps for both actuators is shown in figure 35.

TABLE 7. Experimental data of I-type and U-type actuators for inductance for ten different air gaps.

| Air Gap (mm)	Inductance (mH)	
	I-Type	U-Type
1	37.776	36.053
2	37.053	35.843
3	36.745	35.313
4	36.087	35.012
5	35.887	34.889
6	35.356	34.465
7	35.076	33.877
8	34.762	33.356
9	34.472	32.865
10	34.224	32.134

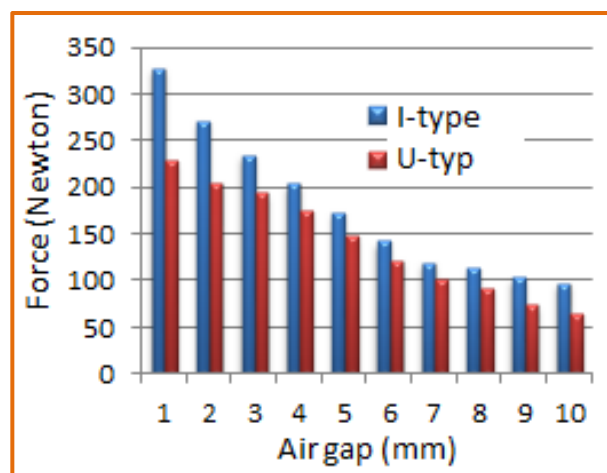**FIGURE 32.** Experimental comparison of inductance profile.
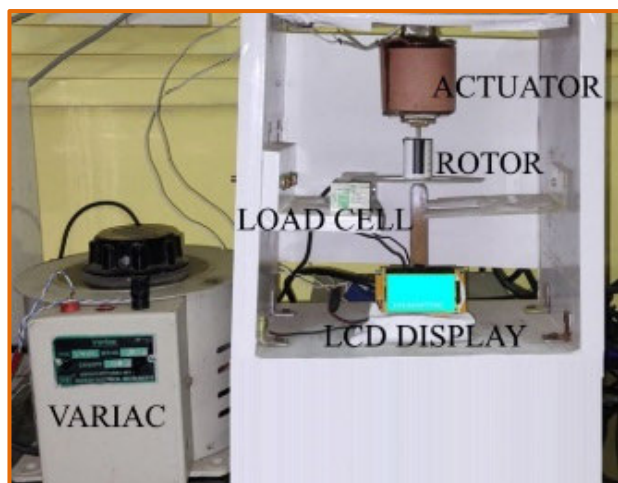
FIGURE 33. Experimental setup for attractive force measurement of I-type actuator using Load cell.

Experimental and analytical result comparison will help determine the better actuator for the Active Magnetic Bearing System. Based on the testing and analytical results, a comparison has been made between inductance and attractive force,
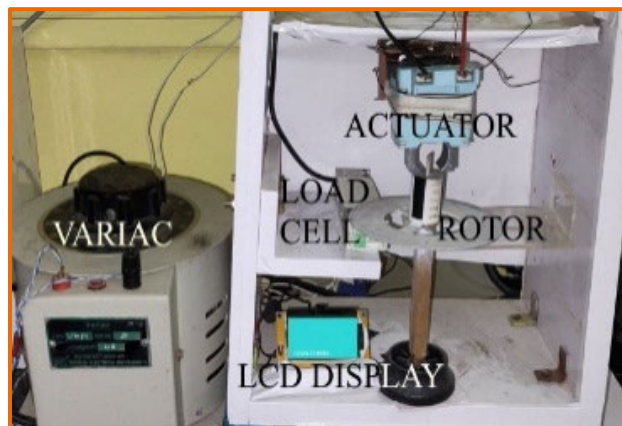
FIGURE 34. Experimental setup for attractive force measurement of U-type actuator using Load cell.

FIGURE 35. Experimental comparison of the attractive force profile.

TABLE 8. Experimental results of I-type and U-type actuators for attractive force in gram and Newton.

Air gap (mm)	Force (N)	
	I-type	U-type
1	327.56	228.12
2	271.33	204.34
3	234.43	193.39
4	203.34	175.79
5	173.23	148.27
6	142.32	121.98
7	118.45	101.77
8	112.29	092.32
9	103.22	073.78
10	97.343	063.32

and the performance graphs are shown in Figures 36 and figure 37.

IV. DESIGN AND TESTING OF I-TYPE AND U-TYPE AMB SYSTEM

The I-type and U-type actuator-based AMB system design has been described in this section. Hardware is set up in accordance with the design data, and the outcomes are shown on a digital oscilloscope.
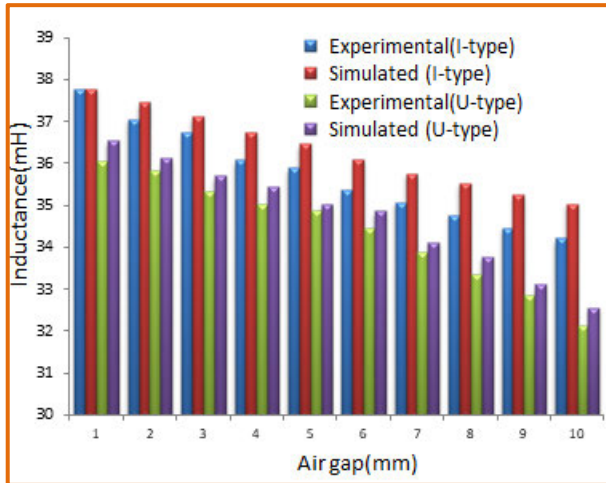
FIGURE 36. Experimental and analytical inductance profile result comparison between I-type and U-type actuators.
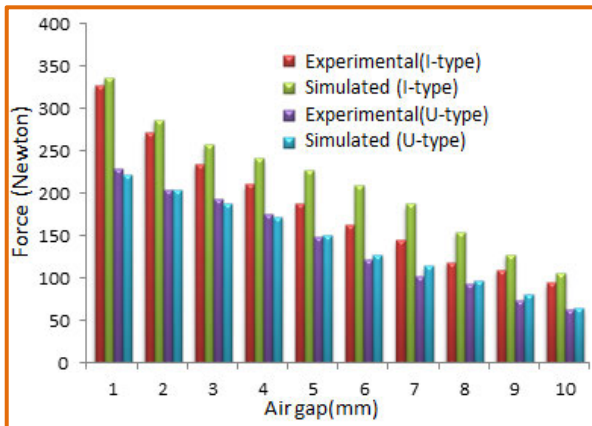

FIGURE 37. Experimental and analytical attractive force profile result comparison between I-type and U-type actuators.

A. DESIGN OF AMB SYSTEM

AMB structures involve multiple components, so correct designing is required to get better performance. Figure 38 depicts the overall closed-loop system. The system's major parts are the current controller, position controller, and power amplifier. The controller and power amplifier design is provided in the following section in accordance with the closed loop system.

1) CURRENT CONTROLLER

The current control loop is shown as a block diagram in Figure 39, with the various subsystems represented as transfer functions.

The current controller, which manages the electromagnetic actuator's current, keeps the rotor in its levitated position. In this work, a proportional plus integral (PI) controller is used to control the coil current. The current controller is given
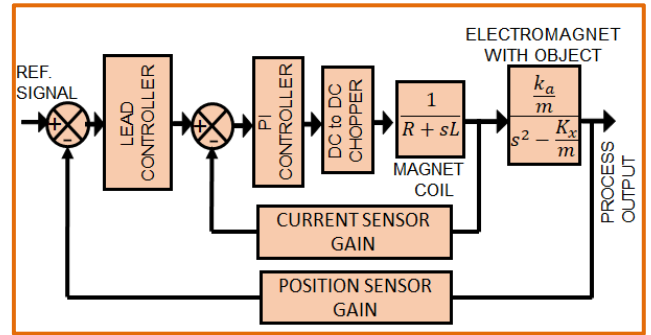

FIGURE 38. Closed loop system of AMB.
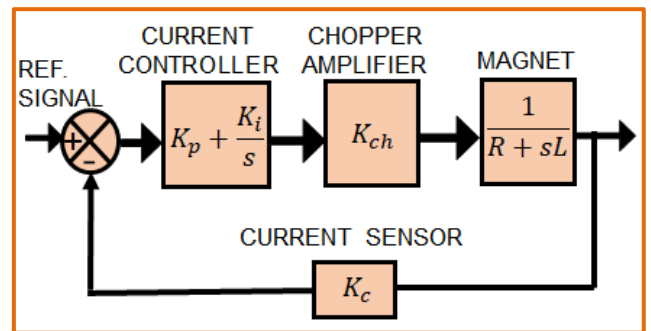
FIGURE 39. Current Loop Block Diagram.
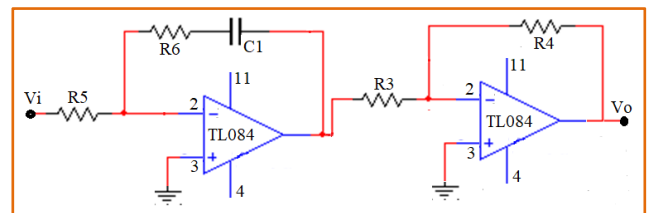
FIGURE 40. Designed PI controller circuit.

a transfer function by

$$G_{cc}(s) = K_p + \frac{K_i}{s} \qquad (1)$$

where the proportional and integral gains, respectively, are $\mathbf{K_P}$ and $\mathbf{K_i}$.

A comparison between the actual current and the reference current is performed in the current control loop. A differential amplifier circuit receives the actual current and scales it (1 amp = 1 volt) using a LEM Hall-effect current sensor. The reference current signal produced by the output of the position controller serves as an additional input to the differential amplifier. A PI controller processes the differential amplifier's output current error signal.

The transfer function of the current controller is described in the following paragraphs and figure 40 depicts its circuit.

$$G_{cc}(s) = \frac{\left(R_6 + \frac{1}{sC_1}\right)}{R_5} = \left(\frac{R_6}{R_5} + \frac{1}{sR_5C_1}\right) \qquad (2)$$

Comparing the integral gain and proportional gain to the PI controller's typical form, $K_p = \frac{R_6}{R_5}$

Consequently, in accordance with the designed current (PI) controller for I-type

$$K_p = \frac{R_6}{R_5} = 4.724 \qquad (3)$$

$$K_i = \frac{1}{R_5 C_1} = 1921.984 \qquad (4)$$

$R_5 = 5.1 k\Omega$ And $R_6 = 24.35 k\Omega$

The nearest standard values for resistors and capacitors have been taken into consideration for the present condition. For adequate attenuation, which enables the control signal to change within the height of the carrier signal, an additional level of gain and sign correction is needed.

Now, the transfer function of the magnetcoil may be determined by taking into account the instantaneous voltage between the magnet winding $v(t)$ and the inductance.

$$\frac{I(s)}{V(s)} = \frac{1}{(R + sL)} \qquad (5)$$

At the nominal working point (5 mm) gap, the I-type coil's transfer function is discovered to be

$$\frac{I(s)}{V(s)} = \frac{1}{(5.8 + 0.179015s)} \qquad (6)$$

Designed current (PI) controller for U-type AMB

$$K_p = \frac{R_6}{R_5} = 4.724 \qquad (7)$$

$$K_i = \frac{1}{R_5 C_1} = 1921.984 \qquad (8)$$

$R_5 = 5.1 k\Omega$ And $R_6 = 24.35 k\Omega$

At the nominal working point (5 mm) gap, the U-type coil's transfer function is discovered to be

$$\frac{I(s)}{V(s)} = \frac{1}{(5.8 + 0.179015s)} \qquad (9)$$

Stability analysis on the current controller (inner closed loop) is carried out with the K_p and K_I values. This analysis is same for both the 'U' type and 'I' type coil because the current controller is same for both of the coil.

When $K_p = 4.724$ and $K_I = 1921.984$ for 5mm air gap the 'U' type and 'I' type coil transfer function is,

$$\frac{I(s)}{V(s)} = \frac{1}{(5.8 + 0.179015s)} \qquad (10)$$

For the above data a program is executed in MATLAB and bode plot is observed as depicted in figure 41

From the figure 41 it is observable that the obtained phase margin (Pm) is 63.80 and the calculated damping ratio (ξ) is 0.638 which lies is the stable range ($0 < \xi < 1$).
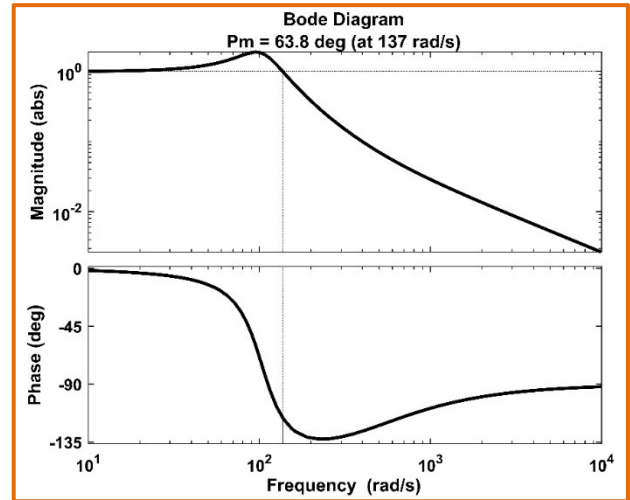

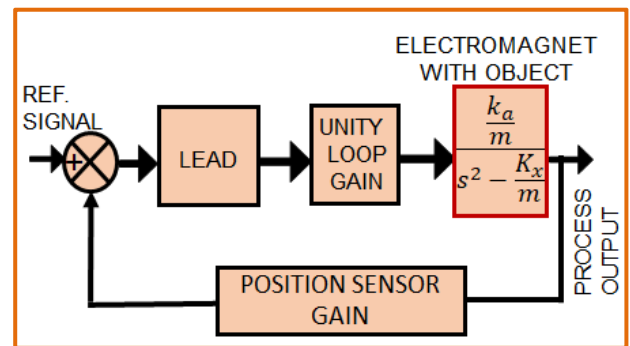**FIGURE 41.** Bode plot for inner current control loop.

FIGURE 42. Simple position control loop block diagram.

2) POSITION CONTROLLER

The position control loop is created after the current controller, which simplifies the position control loop's design by replacing of the position control loop by replacing out the current loop with a single unity gain block (Fig.41). Using a first-order model, the faster inner loop dynamics can be ignored, or approximated while creating the slower position loop controller. The range of the position loop controller's parameters can be understood in this way. To obtain more accurate values of the outer loop controller parameters, however, in order to achieve the desired response, it is always advantageous to take into account the whole model of the inner loop if the order of the inner loop is not high. The simplified position control loop block diagram shown in Figure 42 is made up of a position controller, a current loop, a levitated system (a plant), and a position sensor.

The models of the various position control loop subsystems must be identified in order to construct the position controller. The following sub-sections define the transfer functions of the various blocks of the position control loop.

To mitigate the effects of high-frequency noise, the lead controller transfer function's pole (Pc) needs to be separated from the other poles along the negative real axis.
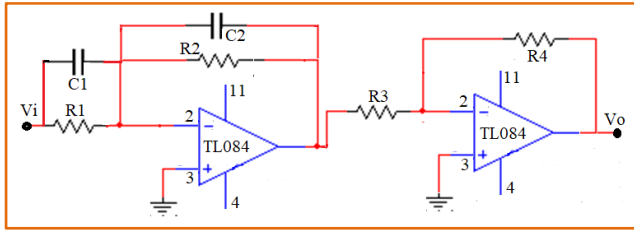
FIGURE 43. Designed circuit diagram of a LEAD controller.

A phase-lead controller with a transfer function is successfully built as a result [23].

$$G(s) = K\left(\frac{s + Z_c}{s + P_c}\right) \tag{10}$$

where

K, Z_c, P_c are compensators gain, zero, and pole

An operational amplifier, along with capacitors, resistors, and other parts, is used to construct a lead controller. The rating of the passive element is computed in order to design the RC circuit. Figure 43 shows the designed circuit diagram of the LEAD controller [24].

The transfer function is

$$\frac{V_0(s)}{V_{in}(s)} = A\left(\frac{s + \frac{1}{R_1 C}}{s + \frac{R_1 + R_2}{R_1 R_2 C}}\right) \tag{11}$$

where, A is gain, and $V_0(s)$, $V_{in}(s)$ are the lead controller's input voltage, and output voltage, respectively.

$$A = 1 + \frac{R_f}{R_0} \tag{12}$$

When we compare these two equations, we obtain the following.

$$Z_c = \frac{1}{R_1 C} \tag{13}$$

$$P_c = \frac{R_1 + R_2}{R_1 R_2 C} \tag{14}$$

As a position controller for an AMB system, a lead controller is designed. Here, a unity current control loop is considered.

Open loop transfer function of 'U' type electromagnet is:

$$G_p(s) = \frac{26.15}{s^2 - 7844.6449}$$

Or

$$G_p(s) = \frac{26.15}{(s + 88.57)(s - 88.57)} \tag{15}$$

And the open loop transfer function of 'I' type electromagnet is:

$$G_p(s) = \frac{13.38}{s^2 - 3369.8025}$$

Or

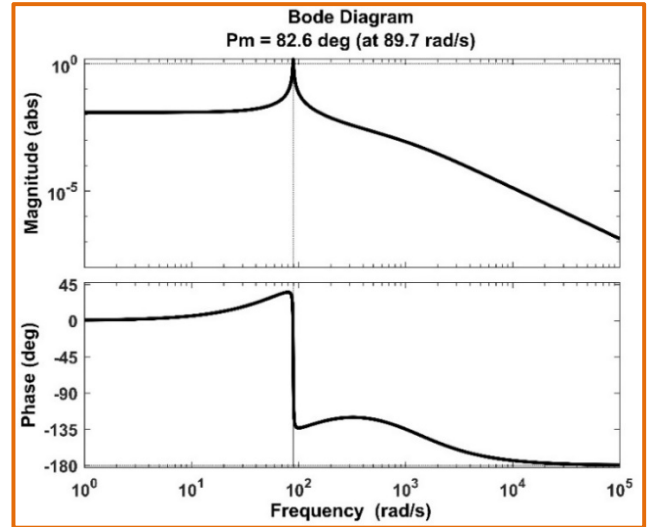$$G_p(s) = \frac{13.38}{(s + 58.05)(s - 58.05)} \tag{16}$$

FIGURE 44. Bode plot of 'U' type coil at 5mm of air gap with lead controller.

From equation 15 and equation 16, it is observable that, open loop transfer function of electromagnet is unstable as it has one pole in the right side of *s* plane. To achieve a proper bearing operation a closed loop is proposed as shown in Figure 38 here the position controller is a lead controller with the transfer function for 'U' type coil. The lead controller transfer function is represented in equation 17,

$$G_{LEAD}(s) = 51.359\left(\frac{s + 88}{s + 1205}\right) \tag{17}$$

And for 'I' type coil the lead controller transfer function is represented in equation 18,

$$G_{LEAD}(s) = 60.183\left(\frac{s + 58}{s + 930}\right) \tag{18}$$

When the inner closed loop is considered as unity, the bode plot of position control loop of 'U' and 'I' type coil with their respective lead controller is obtained to analyze the stability of the system. The bode plot for 'U' and 'I' type coil are depicted in Figure 44 and Figure 45 respectively [25], [26].

From the figure 44 and figure 45, it is clear that the attained phase margin (Pm) is in the range of stable range ($0 < \xi < 1$). As, for 'U' type coil the damping ratio (ξ) is 0.826 and for 'I' type the phase margin is 0.837.

As the position of the rotor get changed from 1mm to 10mm the variation in the step response is depicted in Figure 46. Here, it can observe that as the position of the rotor from the electromagnet is increasing the speed of response gets decreased. This continuous plot of step responses of all the considered air gap shows the precision in performance of the designed closed loop system. further, if the position of the rotor is decreased the system follows the same response corresponding to its air gap value.

In order to obtain the speed of response of the proposed closed loop system with lead controller as a position controller. Step response for all the considered air gaps (from
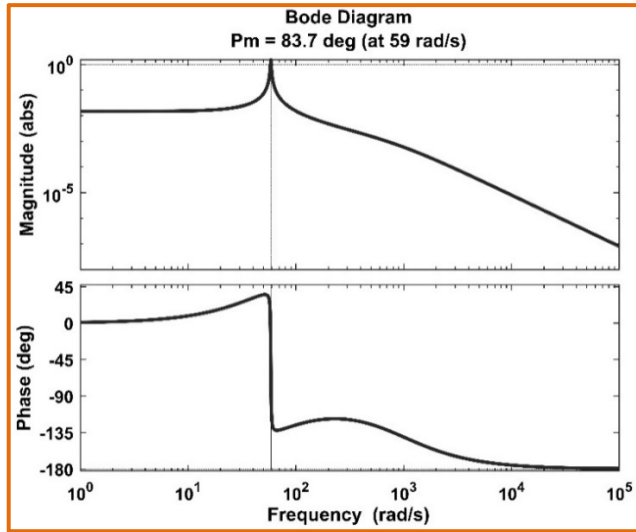
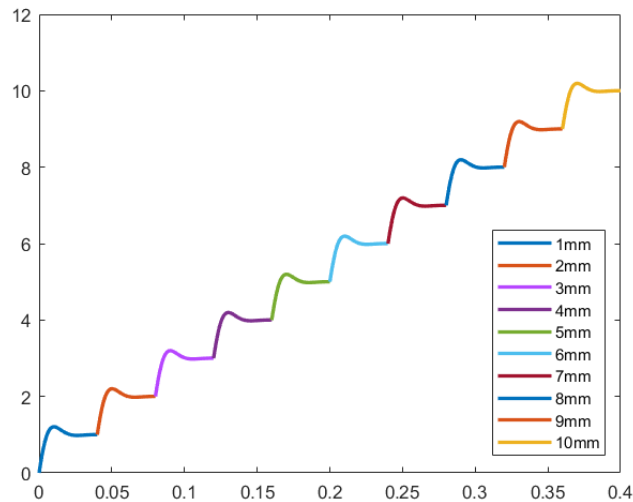**FIGURE 45.** Bode plot of 'I' type coil at 5mm of air gap with lead controller.

FIGURE 46. Continuous step response at different air gap.

FIGURE 47. Step responses for all air gap.

TABLE 9. Settling time and percentage overshoot data obtain from transient state analysis for all air gaps.

Air gap	%Overshoot	Settling Time(sec)
1mm	16%	0.00537
2mm	16%	0.00728
3mm	16%	0.00929
4mm	16%	0.01007
5mm	16%	0.0120
6mm	16%	0.0126
7mm	16%	0.0156
8mm	16%	0.0164
9mm	16%	0.0188
10mm	16%	0.0196
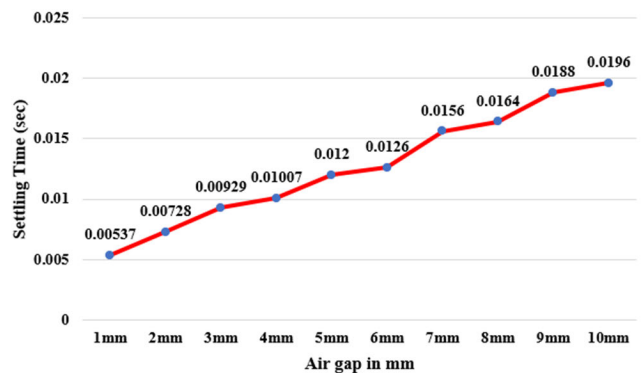
FIGURE 48. Variation in settling time with respect to air gap value.

1mm to 10mm) is plotted as shown if Figure 47 on a single X-Y axis. Where X-axis represents time and Y- axis represents amplitude of the response. Transient state analysis parameters are observed for all of the step responses and to study the speed of response of controller, settling time for a fixed value of percentage overshoot is obtained as listed in Table 9.

Data of the Table shows that increasing the air gap leads to increased settling time, like for 10mm air gap the settling time is 19.6ms and for 1mm the air gap is 5.37ms. this is because as the rotor moves farther to the electromagnet it requires more magnetic force to get hovering which results in increased settling time and vice versa.

To get a clear understanding, the above Table is plotted as a line chart as depicted in Figure 48. This Figure 48 shows that the variation between the settling time and air gap is almost linear in shape and with this lead controller the response of the system is only 19.6ms for 10mm air gap value.

Precision of air gap control of the proposed system is necessary to know how precisely the controller performed. Step response for transfer function of 5.01 mm to 5.04 mm is presented in figure 49 and the step response for transfer function of 5.01 mm to 5.04 mm for a duration of 0 - 0.014 sec,
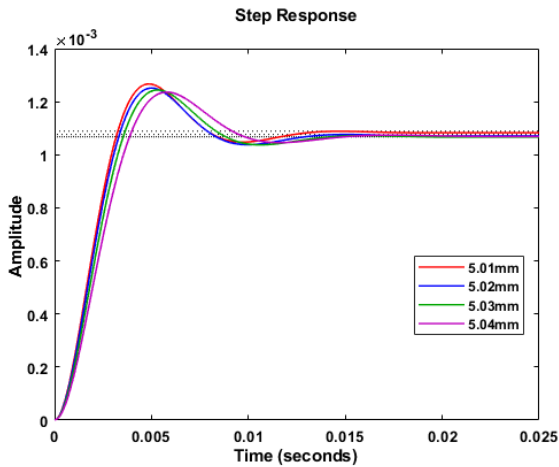
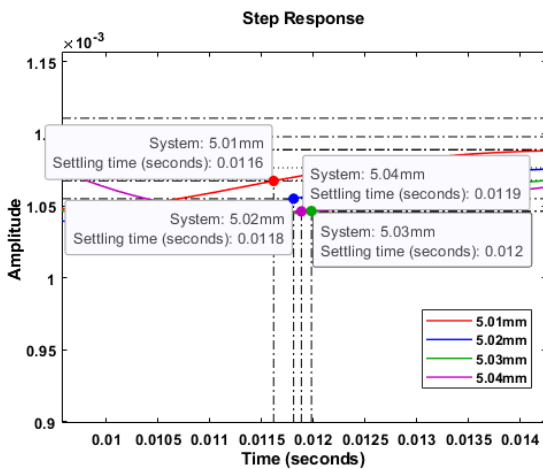**FIGURE 49.** Step response for transfer function of 5.01 mm to 5.04 mm.

FIGURE 50. Step response for transfer function of 5.01 mm to 5.04 mm for a duration of 0 - 0.014 sec, showing settling time (sec) for each case.

TABLE 10. Speed of response for the 5mm air gap control.

Air gap (mm)	Settling Time
5.01	0.0116
5.02	0.0118
5.03	0.0119
5.04	0.0120

showing settling time (sec) for each case is presented in figure 50.

The table 10 shows the speed of response for the particular air gap. From the data it is observed that the proposed controller is very precise in the air gap control.

3) POWER AMPLIFIER

The power circuit in this instance is a single switch-based switched-mode converter circuit. Figure 51 depicts the suggested power circuit diagram. For the figure 51, a hardware model is constructed and shown in figure 52.
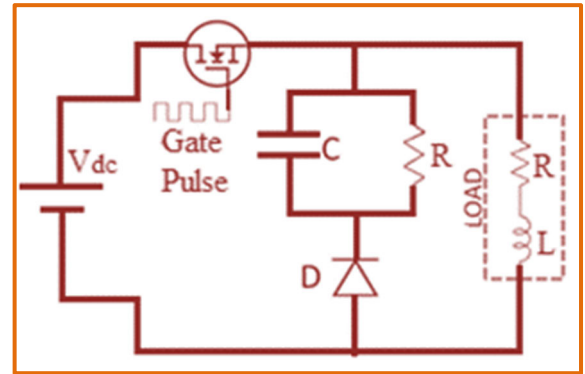
FIGURE 51. Designed amplifier circuit for proposed AMB system.
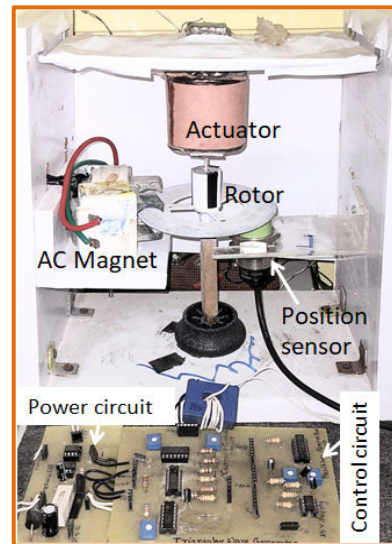
FIGURE 52. Hardware arrangement of I-type actuator-based active magnetic bearing.

The transfer function for this amplifier is as follows:

$$G_{ch}(s) = \frac{K_{ch}}{1 + T_c} \qquad (19)$$

By removing the tiny time constant T_c, the power amplifier's transfer function is subsequently reduced to a straightforward gain.

$$G_{ch} = \frac{dc\ link\ voltage}{control\ voltage} = \frac{V_{dc}}{V_{cm}} \qquad (20)$$

B. TESTING OF U-TYPE AMB SYSTEM

Experimental observation of I-type and U-type active magnetic bearing systems is prepared and the rotor speed is observed.

1) HARDWARE MODEL OF I-TYPE AMB SYSTEM

In the experimental setup of the AMB system, an I-type actuator is used as an electromagnet and the rotor is of disc type. The complete arrangements depicted in Figure 52.
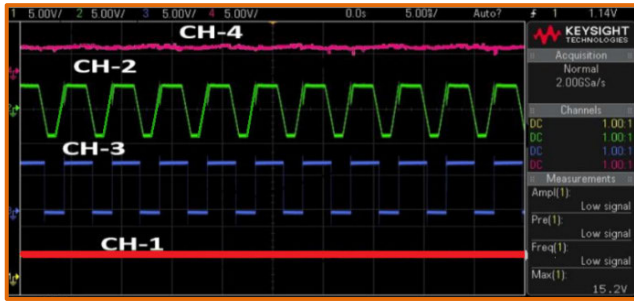
FIGURE 53. CH-1= Position sensor signal; CH-2= Coil voltage; CH-3= Gate pulse and CH-4= Coil current for I-type AMB.

FIGURE 54. Hardware arrangement of U-type actuator-based active magnetic bearing.

FIGURE 55. CH-1= Position sensor signal; CH-2= Coil voltage; CH-3= Gate pulse and CH-4= Coil current for U-type AMB.

FIGURE 56. Hardware output of unity step pulse (pink), the step response of I-type AMB (blue), and step response of U-type AMB (yellow).

In the experimental setup, the position sensor is placed below the rotor to sense the actual position of the rotor. The corresponding signal is fed to the controller for further controlling the action.

Test output for the I-type AMB is shown in figure 53. In this figure position sensor signal, coil voltage, gate pulse, and coil current is presented.

2) HARDWARE MODEL OF U-TYPE AMB SYSTEM
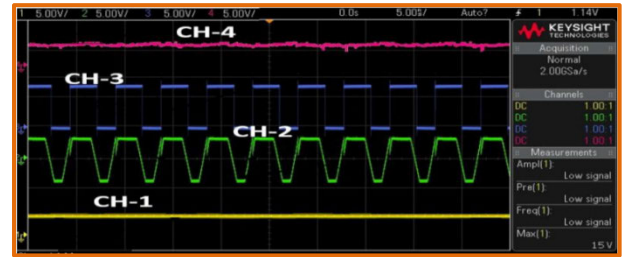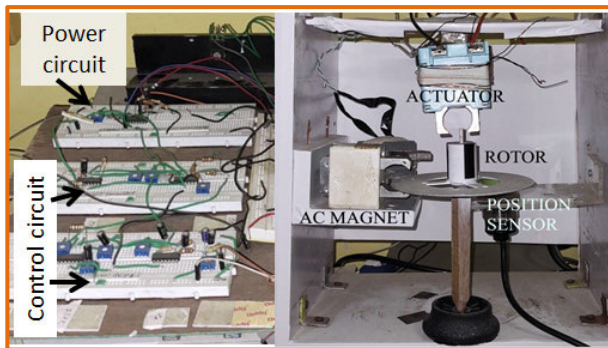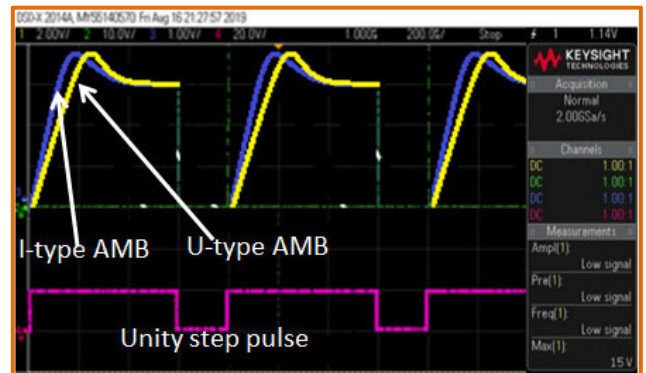For the U-type actuator, the hardware setup is made as portrayed in figure 54. The location of the position sensor, and controlling circuit is the same as the I-type actuator.

The experimental output of the U-type AMB system is presented in figure 55. By connecting a digital oscilloscope performance of the position sensor signal, coil voltage, gate pulse, and coil current is presented.

Further, the transient state behaviour of the experimental model of AMB is observed for the design presented in 4.1 subsections. The corresponding output is displayed in figure 56, where the step response in blue color represents the I-type AMB with an overshoot of almost 13.5% and the response in yellow color represents the U-type AMB with an overshoot of almost 15%. The test data of transient response is presented in table 11.

V. SPEED COMPARISON OF I-TYPE AND U-TYPE AMB
The arrangement presented in figure 52 and figure 54 is made to analyze the rotating speed of the rotor for the I-type and U-type AMB systems.

TABLE 11. The test data of transient response.

Actuator	Overshoot	Peak time (sec)	Rise Time (sec)	Settling Time (sec)	Steady state error
I-type	14.56 %	0.00156	0.00051	0.0055	0.0010
U-type	14.10 %	0.00546	0.00245	0.0120	0.0010

A similar type of rotating system has been employed for both systems. In the space between the series and shunt magnets, the cylinder-mounted aluminium disc is positioned. The shunt electromagnet generates a pulsing magnetic field that penetrates the aluminium disc and eddy currents generated. The interaction of the two magnetic fields and eddy currents creates a driving torque in the disc. The rotational speed of I-type and U-type active magnetic bearings is observed and recorded for different input voltage values; a detailed discussion is given below.

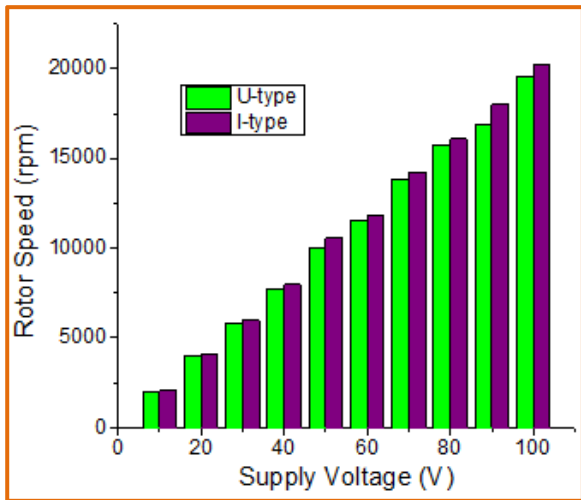### A. ROTATIONAL SPEED OF I-TYPE AND U-TYPE AMB
The rotational speed of the rotor can be controlled by controlling the supply of the shunt magnet. The shunt magnet is energised by supplying the variable ac through a variac. Ten different voltages are provided to the magnet from 10V to 100V, and the tachometer's observed speed for both systems is tabulated in table 12. From this measurement, it is seen that

TABLE 12. The rotational speed of AMB (rpm) in different input voltage.

Input voltage	The rotational speed of U-type AMB (rpm)	The rotational speed of I-type AMB (rpm)
10	1998	2033
20	4021	4122
30	5812	5945
40	7723	7952
50	9998	10563
60	11522	11822
70	13808	14243
80	15774	16073
90	16880	17982
100	19574	20235

FIGURE 57. Speed curve of I-type and U-type active magnetic bearing system.

FIGURE 58. Plot for voltage and current and apparent power versus time during AMB control and divide by suspended mass (Kg) for I-type.

FIGURE 59. Plot for voltage and current and apparent power versus time during AMB control and divide by suspended mass (Kg) for U-type.
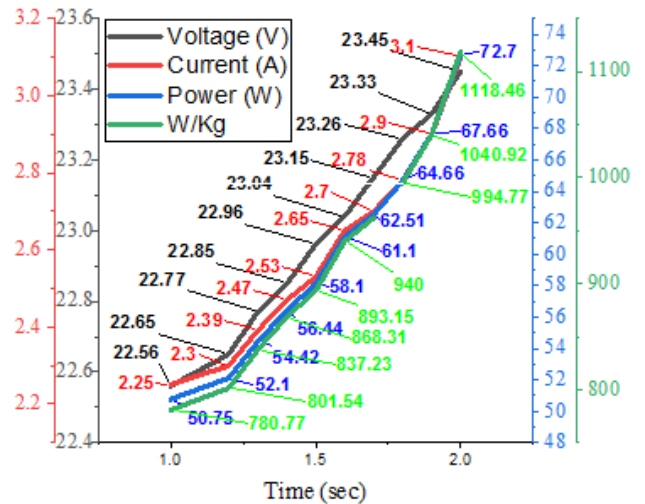
for 10V, 1998 rpm speed is observed in the tachometer for the U-type AMB system and 2033 rpm speed is observed in the tachometer for the I-type AMB system, and 100V 19574 rpm speed for U-type AMB and 20235 rpm speed for I-type AMB is observed. Depending upon the data characteristics graph is plotted and represented in figure 57.

To illustrate the practicality of the actuators in an AMB system, plot of the voltage and current waveforms, as well as the apparent power versus time during AMB control, and divide by the suspended mass (in kg) is presented. This will provide an insight into the amount of power required to control the AMB system and its practicality in terms of power consumption.

For I-type, the voltage during control vary from 20.36 V to 21.54 V and the current vary from 2.15 A to 2.7 A for a 0.065 kg suspended mass. The power curve can be calculated as the product of the voltage and current, resulting in an apparent power of 43.77 W to 58.16 W. Dividing these values by the suspended mass (0.05 kg) gives us an apparent power per kg of 780.77 W/kg to 1118.46 W/kg. Voltage and current and apparent power versus time during AMB control and divide by suspended mass (Kg) is presented in figure 58.

For U-type, the voltage during control vary from 22.56 V to 23.45 V and the current vary from 2.25 A to 3.1 A for a 0.065 kg suspended mass. The power curve can be calculated as the product of the voltage and current, resulting in an apparent power of 50.75 W to 72.7 W. Dividing these values by the suspended mass (0.065 kg) gives us an apparent power per kg of 780.77 W/kg to 1118.46 W/kg. Voltage and current and apparent power versus time during AMB control and divide by suspended mass (Kg) is presented in figure 59.

VI. CONCLUSION

I-type and U-type actuator-based Active Magnetic Bearings have been designed and fabricated in this manuscript. Initially, both the actuators are examined with the assistance of ANSYS Maxwell FEM software for analytical analysis (inductance profile and force profile) and hardware test by

using the ac test (inductance profile) and load cell test (attractive force profile). After all this analysis, AMB systems are designed for both actuators. A PI controller is used for the current controller, and the LEAD controller is used for the position controller for both AMB systems. According to the designed data, simulation and hardware analysis have been performed, and stable outputs are observed for the current and position controller response.

After achieving the stable rotor levitated position for both the AMB system, a rotational system has been designed to rotate the rotor, and at low input voltage, a higher rotational speed is observed. Finally, the rotor speed is recorded in the tachometer for ten different voltages for both systems. At 100V, a 19574 rpm speed is observed for the U-type AMB system, and a 20235 rpm speed is observed for the I-type AMB system. The plot of voltage and current and apparent power versus time during AMB control and divide by suspended mass (Kg) is presented to illustrate the practicality of the actuator. This type of system further can be implemented for high-speed machining applications.

CONFLICT OF INTEREST
The authors declare no conflicts of interest to disclose.

REFERENCES

[1] S. Gerhard, B. Hannes, and T. Alfons, *Active Magnetic Bearings: Basics, Properties and Applications of Magnetic Bearings*. Zürich, Switzerland: VDF Hochschulverlag AG an der ETH Zürich, 1994.

[2] S. Gerhard, B. Hannes, and T. Alfons, *Magnetic Bearings: Theory, Design, and Application to Rotating Machinery*. Cham, Switzerland: Springer, 2009.

[3] S. Debnath and P. K. Biswas, "Design, analysis, and testing of I-type electromagnetic actuator used in single-coil active magnetic bearing," *Electr. Eng.*, vol. 103, no. 1, pp. 183–194, Feb. 2021.

[4] J. You, R. Wang, H. Chen, F. Chen, and H. Liang, "A novel design of the rotary electromagnetic actuator and the analysis of critical demagnetization state for its permanent magnet," in *Proc. IEEE Int. Magn. Conf. (INTERMAG)*, Apr. 2017, pp. 1.

[5] T. Du, H. Geng, Y. Zhang, H. Lin, Y. Li, and L. Yu, "Exact analytical method for active magnetic bearings with rotor eccentricity," *IEEE Trans. Magn.*, vol. 55, no. 12, pp. 1–12, Dec. 2019.

[6] Y. Xu, Q. Shen, Y. Zhang, J. Zhou, and C. Jin, "Dynamic modeling of the active magnetic bearing system operating in base motion condition," *IEEE Access*, vol. 8, pp. 166003–166013, 2020.

[7] H. Jiang, Z. Su, and D. Wang, "Analytical calculation of active magnetic bearing based on distributed magnetic circuit method," *IEEE Trans. Energy Convers.*, vol. 36, no. 3, pp. 1841–1851, Sep. 2021.

[8] A. Heya, K. Hirata, N. Niguchi, and A. Nakajima, "Triaxial active control magnetic bearing with asymmetric structure," *IEEE Trans. Ind. Appl.*, vol. 57, no. 5, pp. 4675–4685, Sep. 2021.

[9] H. Sun, D. Jiang, and J. Yang, "Synchronous vibration suppression of magnetic bearing systems without angular sensors," *CES Trans. Electr. Mach. Syst.*, vol. 5, no. 1, pp. 70–77, Mar. 2021.

[10] S. Xu and J. Fang, "A novel conical active magnetic bearing with claw structure," *IEEE Trans. Magn.*, vol. 50, no. 5, pp. 1–8, May 2014.

[11] S.-L. Chen and C.-T. Hsu, "Optimal design of a three-pole active magnetic bearing," *IEEE Trans. Magn.*, vol. 38, no. 5, pp. 3458–3466, Sep. 2002.

[12] S.-L. Chen and C.-C. Weng, "Robust control of a voltage-controlled three-pole active magnetic bearing system," *IEEE/ASME Trans. Mechatronics*, vol. 15, no. 3, pp. 381–388, Jun. 2010.

[13] S. Chen, S. Lin, and C. Toh, "Adaptive unbalance compensation for a three-pole active magnetic bearing system," *IEEE Trans. Ind. Electron.*, vol. 67, no. 3, pp. 2097–2106, Mar. 2020.

[14] A. Noshadi, J. Shi, W. S. Lee, P. Shi, and A. Kalam, "System identification and robust control of multi-input multi-output active magnetic bearing systems," *IEEE Trans. Control Syst. Technol.*, vol. 24, no. 4, pp. 1227–1239, Jul. 2016.

[15] S.-L. Chen, "Nonlinear smooth feedback control of a three-pole active magnetic bearing system," *IEEE Trans. Control Syst. Technol.*, vol. 19, no. 3, pp. 615–621, May 2011.

[16] S.-L. Chen, S.-H. Chen, and S.-T. Yan, "Experimental validation of a current-controlled three-pole magnetic rotor-bearing system," *IEEE Trans. Magn.*, vol. 41, no. 1, pp. 99–112, Jan. 2005.

[17] N. Schofield, A. Lonsdale, and A. Y. Hodges, "Static and dynamic electromagnetic actuator designs for a fluctuating force module (FFM) calibration test facility," *IEEE Trans. Magn.*, vol. 40, no. 4, pp. 2074–2076, Jul. 2004.

[18] P. Raghunathan and E. Logashanmugam, "Design and testing of electromagnetic actuator used in axial active magnetic bearing," in *Proc. Int. Conf. Control, Instrum., Commun. Comput. Technol. (ICCICCT)*, Dec. 2016, pp. 809–812.

[19] S. Debnath, "Study and analysis on some design aspects in single and multi-axis active magnetic bearing (AMB)," *J. Appl. Res. Technol.*, vol. 19, no. 5, pp. 448–471, Oct. 2021.

[20] B. V. Jayawant, "Electromagnetic suspension and levitation techniques," *Proc. Roy. Soc. A, Math., Phys. Eng. Sci.*, vol. 416, pp. 245–320, Jan. 1988.

[21] S. Lim and S. Min, "Design optimization of permanent magnet actuator using multi-phase level-set model," *IEEE Trans. Magn.*, vol. 48, no. 4, pp. 1641–1644, Apr. 2012.

[22] J. Laldingliana, S. Debnath, and P. K. Biswas, "Fem software based 2-D and 3-D construction and simulation of single and double coils active magnetic bearing," *Int. J. Innov. Technol. Exploring Eng.*, vol. 8, no. 11, pp. 665–675, Sep. 2019.

[23] S. K. Dash and K. S. Swarup, "Design optimization of single-axis thrust magnetic bearing actuator," *J. CPRI*, vol. 10, pp. 1–12, Jan. 2014.

[24] L. V. Rao and S. K. Kakoty, "Design of compact active magnetic bearing," *Int. J. Appl. Sci. Eng. Res.*, vol. 3, no. 3, pp. 741–754, 2014.

[25] S. Debnath, P. K. Biswas, and J. Laldingliana, "Analysis and simulation of PWM based power amplifier for single axis active magnetic bearing (AMB)," in *Proc. IEEE Transp. Electrific. Conf.*, Pune, India, Dec. 2017, pp. 1–5.

[26] D. Sukanta and K. B. Pabitra, "Advanced magnetic bearing device for high-speed applications with an I-type electromagnet," *Electr. Power Compon. Syst.*, vol. 48, pp. 1862–1874, May 2021.

UPAMA DAS received the B.Tech. degree from WBUT, India, the M.Tech. degree from NIT Agartala, Tripura, India, and the Ph.D. degree in electrical engineering from the National Institute of Technology Mizoram (NIT Mizoram), Aizawl, India.

She is currently an Assistant Professor of electrical and electronics engineering with NIT Mizoram.

SUKANTA DEBNATH received the B.Tech. degree from WBUT, India, the M.Tech. degree from NIT Agartala, Tripura, India, and the Ph.D. degree in electrical engineering from the National Institute of Technology Mizoram (NIT Mizoram), Aizawl, India.

He is currently an Assistant Professor of electrical and electronics engineering with NIT Mizoram.

SURAJ GUPTA (Graduate Student Member, IEEE) was born in Uttar Pradesh, India, in 1991. He received the B.Tech. degree from UPTU, India, and the M.Tech. degree from the National Institute of Technology Mizoram (NIT Mizoram), Aizawl, India, where he is currently pursuing the Ph.D. degree with the Department of Electrical and Electronics Engineering.

PABITRA KUMAR BISWAS (Member, IEEE) received the B.Tech. degree from the Asansol Engineering College, WBUT, India, the M.E. degree in EE power electronics and drives from Bengal Engineering and Science University, West Bengal, India, in 2007, and the Ph.D. degree in electrical engineering from the National Institute of Technology, Durgapur, India, in 2013.

He was the HoD of the EEE Department, from February 2015 to August 2019. He is currently an Assistant Professor and the HoD in electrical and electronics engineering with the National Institute of Technology Mizoram, India. He has about 14 years of academic as well as research experience. He has completed one DST-SERB Project. He has guided five Ph.D. students and more than ten M.Tech. students and ten more are pursuing their research at present. He has reviewed papers in reputed international conference and journals. He has successfully organized a GIAN course, two short term course, and a FDP (ATAL). He has published a numbers of research papers in national/international conference and records/journals. He has a book and more than six book chapters and filed three patents. His research interests include electromagnetic levitation systems, active magnetic bearing, power electronics converters, PMSM and BLDC motor drives, electric vehicles, and renewable energy.

Dr. Biswas is a member of the Institute of Engineers and the International Association of Engineers. He is also a fellow of the SAS Society (FSASS). He has received the Best Paper Award and the Best Researcher Award from the International Scientist Awards on Engineering, Science and Medicine.

THANIKANTI SUDHAKAR BABU (Senior Member, IEEE) received the B.Tech. degree from Jawaharlal Nehru Technological University, Ananthapur, India, in 2009, the M.Tech. degree in power electronics and industrial drives from Anna University, Chennai, India, in 2011, and the Ph.D. degree from VIT University, Vellore, India, in 2017.

He was a Postdoctoral Researcher with the Department of Electrical Power Engineering, Institute of Power Engineering, University Tenaga Nasional (UNITEN), Malaysia. He is currently an Associate Director of Research and Development, and an Associate Professor with the Department of EEE, Chaitanya Bharathi Institute of Technology, Hyderabad, India. He has published more than 150 research articles in various renowned international journals. His research interests include the design and implementation of solar PV systems, renewable energy resources, power management for hybrid energy systems, storage systems, fuel cell technologies, electric vehicle, and smart grids. He has been acting as an Editorial Board Member and a Reviewer of various reputed journals, such as the IEEE, IEEE Access, IET, Elsevier, EPCS, and Taylor & Francis. He has received the Vice-Chancellors Research Excellence Award from Osmania University, Hyderabad, in 2023.

NNAMDI I. NWULU (Senior Member, IEEE) is currently a Full Professor with the Department of Electrical and Electronic Engineering Science, University of Johannesburg, and the Director of the Centre for Cyber Physical Food, Energy and Water Systems (CCP-FEWS). His research interests include the application of digital technologies, mathematical optimization techniques, and machine learning algorithms in food, energy, and water systems. He is a Senior Member of the South African Institute of Electrical Engineers (SMSAIEE) and a Y-Rated Researcher by the National Research Foundation of South Africa. He is the Editor-in-Chief of the *Journal of Digital Food Energy and Water Systems* (JDFEWS) and an Associate Editor of *IET Renewable Power Generation* (IET-RPG) and *African Journal of Science, Technology, Innovation and Development* (AJSTID). He is a Professional Engineer registered with the Engineering Council of South Africa (ECSA).

● ● ●